



ASME Journal of Micro- and Nano-Manufacturing Online journal at:

https://asmedigitalcollection.asme.org/micronanomanufacturing



Obehi G. Dibua

Department of Mechanical Engineering, University of Texas at Austin, Austin, TX 78712

Farzana Tasnim

Department of Mechanical Engineering, University of Texas at Austin, Austin, TX 78712

Aaron Liao

Department of Mechanical Engineering, University of Texas at Austin, Austin, TX 78712

Joshua Grose

Department of Mechanical Engineering, University of Texas at Austin, Austin, TX 78705

Dipankar Behera

Department of Mechanical Engineering, University of Texas at Austin, Austin, TX 80020

Chee S. Foong

NXP Semiconductors, Austin, TX 78759

Michael Cullinan

Department of Mechanical Engineering, University of Texas at Austin, Austin, TX 78712

Predicting Electrical Resistivity of Sintered Copper Nanoparticles From Simulations for the Microscale Selective Laser Sintering Process

One of the main challenges facing the expansion of Additive Manufacturing (AM) is the minimum feature sizes which these processes are able to achieve. Microscale Selective Laser Sintering (µ-SLS) is a novel Additive Manufacturing process created to meet this limitation by precisely laser sintering nanoparticles to give a better control over feature sizes. With the development of this new process, there is a concurrent need for models, which can predict the material properties of the sintering nanoparticles. To this end, this paper presents a novel simulation created to predict the electrical resistivity of sintered copper nanoparticles. Understanding the electrical resistivity of nanoparticles under sintering is useful for quantifying the rate of sintering and has applications such as predicting how the nanoparticles will fuse together when subjected to laser irradiation. Such a prediction allows for in situ corrections to be made to the sintering process to account for heat spreading beyond the intended laser irradiation targets. For these applications, it is important to ensure that the predictions of electrical resistivity from the simulations are accurate. This validation must be done against experimental data and since such experimental data does not currently exist, this paper also presents electrical resistivity data for the laser sintering of copper nanoparticles. In summary, this paper details the simulation methodology for predicting electrical resistivity of laser-sintered copper nanoparticles as well as validation of these simulations using electrical resistivity data from original sintering experiments. The key findings of this work are that the simulations can be used to predict electrical resistivity measurements for sintering of actual copper nanoparticles when the copper nanoparticles do not include other materials such as polymer coatings. [DOI: 10.1115/1.4064389]

1 Introduction

The increasing demands on computational resources have led to a need for a matching reduction in the sizes of transistors so that more transistors can be packed into the same area on a chip [1,2]. A promising solution to meet this limitation is to utilize 3D packaging in the chip fabrication process [3,4]. AM is a fabrication process where parts are built directly from a computer aided design without the need for part specific manufacturing tools. The properties inherent in Additive Manufacturing make it ideally suited for creating 3D structures in a microchip. However, most commercially available metal AM processes have minimum feature sizes of the order of hundreds of micrometers [5–7]. This limitation prevents the use of AM technologies for chip fabrication in the micro-electronics industry where small feature sizes are critical. μ -SLS is a novel AM process, which has been created to meet this limitation and allow for part creation on the sizes needed for the micro-electronics industry.

Contributed by the Manufacturing Engineering Division of ASME for publication in the JOURNAL OF MICRO- AND NANO-MANUFACTURING. Manuscript received June 18, 2023; final manuscript received December 10, 2023; published online January 24, 2024.

Selective laser sintering (SLS) is a powder-based AM process. In this process, a layer of powder is spread over a substrate. A laser rasters over the powder bed, following the path prescribed by the computer aided design file. This laser provides the heat source responsible for fusing the powder particles together into a solid part [7,8]. Like SLS, μ -SLS is an AM process where energy from a laser is used to fuse the particles together into a full part. Unlike SLS though, μ -SLS uses the sintering of nanoparticles to give a better control on the feature sizes. Because the resolution of the part is restricted to the size of the particles that make up the part, the particles have to be smaller than the desired resolution. Therefore, to achieve submicron resolution the particles that make up the part have to be nanosized. In addition to the nanoparticles, a digital micromirror device array is used to achieve spot sizes of about 1 μ m [9–12].

One of the challenges faced with precisely building parts from the μ -SLS process is the presence of heat affected zones (HAZ), which form around laser irradiated spots during sintering. When a laser is directed onto a spot on the powder bed, heat spreads from the irradiated spots to the surrounding areas. The sintered area outside of the irradiated spot is known as the HAZ and the presence of HAZs

lead to imprecision in the sintering area, making it difficult to attain near-net shaped parts. To correct for the HAZs, which are formed during sintering, it is important to be able to make predictions of how the HAZs are going to form when a laser source is applied. To this end, models of the μ -SLS sintering process need to be created to predict how heat spreads in the powder bed. However, in order to model the heat spread during μ -SLS sintering, it is first important to be able to model how nanoparticles sinter when subjected to a thermal source.

The model of nanoparticles sintering in a powder bed has been created and is presented in [13]. This model uses the phase field modeling (PFM) approach to model how the nanoparticles sinter. PFM is a diffuse interface approach, which tracks the evolution of the particles in the bed using phase field variables which are related to microscopic parameters. To simulate this process, first a simulation bed of nanoparticles is created using a Discrete Element Method model to match a single layer of deposited nanoparticles from experiments, where each particle in the bed is approximated as a sphere having an average radius of 100 nm. The spherical particles are allowed to interact, subject to collision, cohesive and gravitational forces, until the particles settle into a steady-state configuration [14,15]. Once this steady-state configuration is achieved, the simulation bed undergoes sintering. Sintering in this PFM simulation is a result of the temporal evolution of the phase field variables driven by a set input temperature. The evolution of the density phase field variable is governed by the Cahn Hilliard equation [16,17] and the order parameter phase field variable by the Ginzburg-Landau equation [18]. The rate at which these variables evolve defines the nanoparticle sintering and is determined by simulation parameters which have been calibrated to correlate to sintering at different temperatures [19].

To reliably use this PFM simulation of the nanoparticles sintering, validation must be done to ensure accurate predictions from the simulation. This validation is done by comparing electrical resistance predictions from the simulations against actual electrical resistance measurements from the μ -SLS system to determine how well the simulations match experiments. This paper presents the methodology to achieve this validation and the resulting findings from the validation process. To perform this validation, electrical resistance metrology tools were developed to measure the resistance of the simulation beds as well as the actual sintered nanoparticle beds, and the data produced from both processes were compared. Additionally, while calibration of the simulation parameters to sintering temperatures has been done for the PFM simulation, there has been no link drawn between simulation parameters and the μ-SLS laser sintering parameters. As such, electrical resistance measurements are performed on the μ -SLS system to bridge this gap, and the results are outlined in this paper.

2 Methodology

2.1 Simulations. A simulation metrology tool was built in Python to measure the resistance in the simulation beds, which result from the PFM sintering simulation in Ref. [20]. Figure 1 shows an

example of the evolution of a sintered bed resulting from the PFM sintering simulation [19].

The resistance metrology tool in [20] uses the modified Reimann-Weber formula [21] in Eq. (1) to determine the resistance in the sintered beds from the simulations. The electrical resistance in each bed comes from two main sources, the neck between the particles that make up the bed and the bulk of these particles. The modified Reimann-Weber formula in Eq. (1) gives the resistivity in the neck between two particles in contact of radii r_1 and r_2 , connected with a neck of radius x

$$\rho_{\text{neck}} = \rho_{\text{bulk}} \left(\frac{r_{\text{avg}}}{x} + \frac{\ln(2r_{\text{avg}}/x)}{\pi} \right) \tag{1}$$

where ρ_{bulk} is the bulk resistivity of the material and $r_{\text{avg}} = \frac{r_1 + r_2}{2}$.

The first step to using Eq. (1) to determine the resistivity between particles is isolating the particles in contact which apply in Eq. (1). This is done in two stages, first by determining if the particles are in close enough proximity for encapsulating spheres drawn around the particles to overlap. For two particles defined by $center_{ji}$ and radius r_i , this overlap test is performed using the following equation:

$$c = \sqrt{\sum_{i=1}^{3} (\operatorname{center}_{1i} - \operatorname{center}_{2i})^{2} - (r_{1} + r_{2})}$$

$$\begin{cases} \text{if } c \leq 0 & \text{particles 1 and 2 are possibly connected} \\ \text{else} & \text{particles 1 and 2 are not connected} \end{cases}$$
(2)

From the narrowed list of particles with overlapping spherical boundaries, a pair of sweeping planes is used to determine if the particles under test are in contact. This process involves sweeping a pair of planes, orthogonal to the line that connects the centers of the particles, from the center of one particle to the center of the other in the direction of the line of contact between the particles. If the particles are in contact, then these sweeping planes, which are separated by a pixel, never have any empty space between them when moving from the center of the first particle to the center of the second

Once it has been determined that the two particles under test are in contact, then the resistance of the neck connecting these particles is calculated. The total resistance of the neck between these contacting particles is calculated as the sum of the resistance of each slice. This is done because of the amorphous form of the necks. The resistance of each slice of the neck between the pixel separated sweeping planes is calculated by approximating each pixel slice as a cylinder of height 1 and radius $r_{\rm slice}$. The radius, $r_{\rm slice}$, is calculated as the furthest distance between a pixel in the pixel slice point cloud and the center of the point cloud. The resistance of the slice is then calculated from the resistivity of that slice, which is derived by plugging in $r_{\rm slice}$ for x in Eq. (1).

After the resistance of the necks is calculated, the necks are sorted into directions based off the direction of the line connecting the particles. When the overall resistance in the bed is calculated, the potential difference is applied across both ends of a single direction,

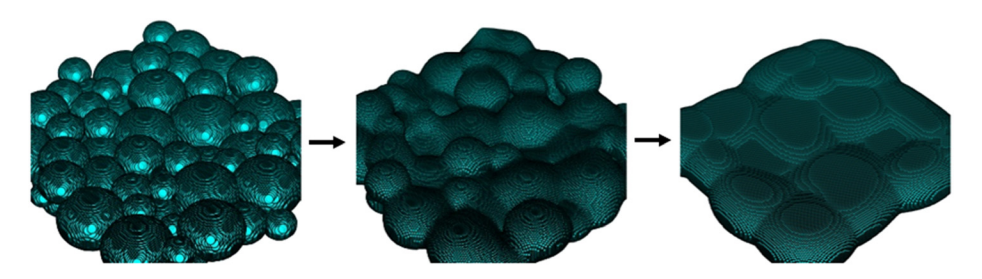


Fig. 1 Evolution of sintering on a two-by-two micrometer bed from the PFM sintering simulation in Ref. [13]

x or y. Since the potential difference drives the movement of electrons, which in turn leads to the current flow through the bed, only current flow in the direction of the potential difference is used. Once the resistance of the neck is calculated, the neck region is cut away from the particles in contact and then the resistance of each of the particles is calculated using the same method as a sum of slices, also due to the amorphous nature of the particles. This gives the resistance in the bulk of the particles.

The resistance in the bulk and in the neck between particles is then used to get a resistance circuit between the particles in contact. For this circuit, each particle has a node at the start of the particle (depicted as Node 1 in Fig. 2), connected to the neck by the resistance of the bulk of the particle, then through the neck region by the resistance of the neck region and then to the other particle through the resistance of the bulk of the second particle as illustrated in Fig. 2.

The procedure for developing this resistance circuit can be summarized in the pseudo-code below:

```
Assign two node numbers to each particle, one to represent the particle's end and one to represent the center
```

Create an empty 3x1 list for the resistance circuit
For each pair of particles in the bed
{
 Determine if the two particles are in contact
 If the particles are in contact
 {
 Extract the neck region between the particles

Calculate the resistance of that neck region
Append the particle center nodes and the neck resistance
value to the resistance circuit list

}
Calculate the bulk resistance of each particle after all neck regions have been removed

Append the particle end node, center node, and bulk resistance value to the resistance circuit list

For each particle in the bed

Determine if the particle is at the edge of the simulation bed If the particle is at an edge, determine if it is at the starting edge of current flow or the ending edge

If at the starting edge

Reassign the particle's end node number to 0 in the resistance circuit list

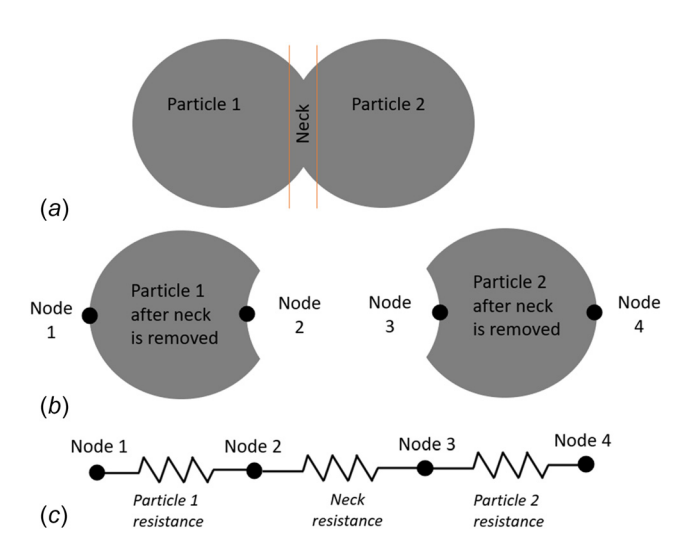


Fig. 2 Creating resistance circuit from two particles in contact. (a) Necking particles. (b) Particles after the neck regions are removed. (c) Equivalent resistance network derived from the particles in (a).

```
If at the ending edge
{
    Reassign the particle's end node number to 1 in the resistance circuit list
    }
}
```

Once this network of connections is established an effective circuit is produced such as shown in Fig. 3. This resistance network, which simply contains the derived resistance circuit list, is sent to the SPICE electronics circuit simulator, which simulates applying a potential difference across the edge nodes provided and measures the current flow through the circuit. The total resistance of the bed is calculated from ohms law as the voltage divided by the current.

2.2 Experiments. The map between resistance and density for copper nanoparticles was derived from performing sintering experiments on copper nanoparticle pellets as presented in Ref. [22]. These experiments were carried out on CI-005 copper nanoparticle ink supplied by NovaCentrix. 2 mL of the ink was placed in a petri dish to dry. Once dry, the dried ink was formed into pellets in crucibles and placed in a furnace to sinter. The density of the pellets of dried nanoparticles was measured from the mass and the volume of the pellets. The density was measured after sintering in the furnace, and then the relative change in density was calculated using these measured density values. The experimental flow for the measurements performed on the copper nanoparticle pellets is shown in Fig. 4.

After sintering of these copper nanoparticle pellets, the electrical resistance of the sintered pellets was also measured using a fourpoint probe setup. The four-point probe setup uses four different contact points to measure the resistance in a circuit, thereby eliminating contact resistance from the resistance values measured [23]. In the four-point probe technique, current is flowed into the material through the outer probes, and the potential difference across the middle probes is measured. The resistance is then calculated using Ohm's law as the ratio of voltage difference to current. However, since the degree of sintering is not even throughout the sintered pellets, the electrical resistance could not be measured using a simple four-point probe setup across the surfaces of the sintered pellets. Instead, a new measuring tool had to be designed to take advantage of the four-point probe resistance measurement setup, while also measuring the resistance through the pellets. The fourpoint probe setup used for carrying out these experiments is shown in Fig. 5.

Once the measurements of the density and the electrical resistance of the sintered copper pellets were concluded, experiments were performed on the μ -SLS system to measure the electrical resistance of the manufactured parts as a function of the laser sintering parameters. These experiments were performed using the same copper nanoparticle ink used for the pellet measurements discussed above. An image of the μ -SLS system is shown in Fig. 6.

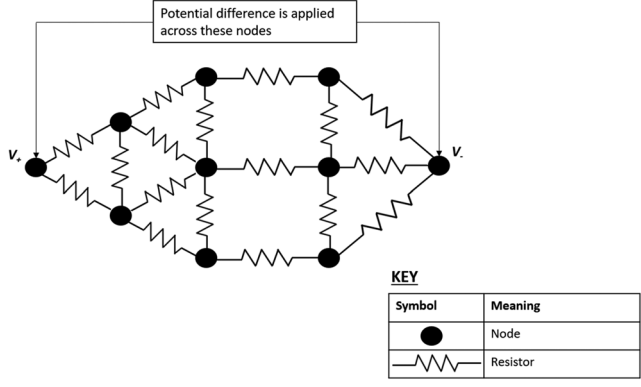


Fig. 3 Example resistance circuit

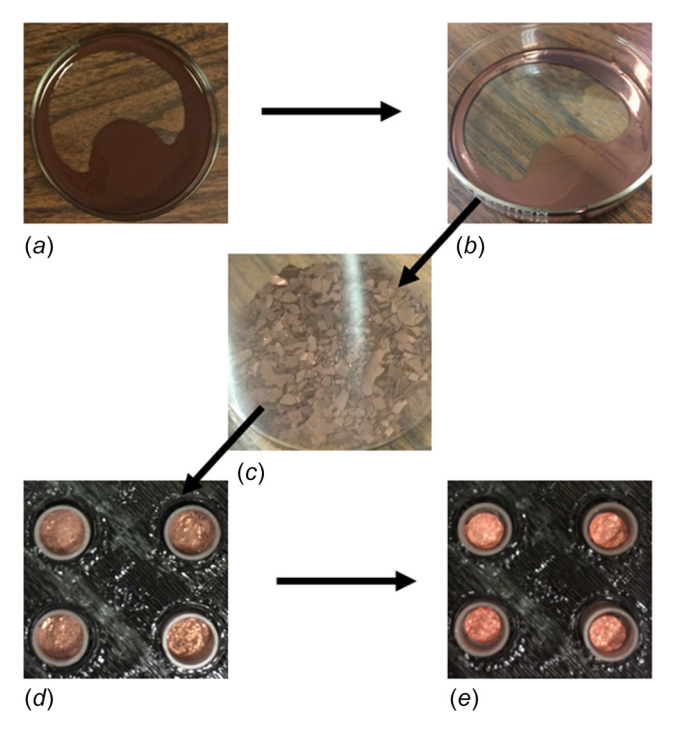


Fig. 4 Experimental procedure. (a) Copper nanoparticle ink. (b) Dried ink. (c) Scraped off dried flakes. (d) Pellets in crucible before sintering. (e) Pellets in crucible after sintering [22].

For these experiments, the copper nanoparticle ink was deposited onto glass substrates and then rectangles were sintered at varying laser exposure times, using the same laser power for sintering. The electrical resistance of these rectangular samples was then measured using a four-point probe setup, and the relationship between electrical resistance and laser exposure time was derived. The results of the pellet experiments as well as the experiments performed on the μ -SLS system are presented and discussed in the Results section.

3 Results and Discussion

3.1 Simulations. The resistance measurement simulation tool was used to calculate the resistance of 6 two-by-two micrometer

beds, and the potential difference was applied to the x and y bounds of each of these beds, giving 12 different resistance curves. The results are presented in Fig. 7. The blue points in Fig. 7 are the raw data points and the yellow lines are curve fits to the upper and lower bounds of the data points. These curve fits encompass over 95% of the data points, giving the uncertainty window for these resistance calculations with the two-by-two micrometer beds. The curve fits were found by breaking the data points into rectangular grids of width 1% density change, which is the x-axis of Fig. 7. The maximum and minimum resistance values within these windows were stored and the upper bound curve was fit to the collection of all the maximum values, and the lower bound fit to the minimum values. The curves were fit to an exponential function of the form in the following equation:

$$R = K_1 e^{-K_2(x+K_3)+K_4} + K_5$$
 (3)

where R in the equation is the electrical resistance, and x is the scaled density change. The results in Fig. 7 show the same trends seen with the one-by-one micrometer beds, with general decreasing resistance with increasing densification in the bed. Figure 7 plots the electrical resistivities calculated from the electrical resistance, and the bulk resistivity is shown in the black dashed line as a reference. The resistivity of the beds approaches the bulk value as the amount of densification increases. The rate at which the results approach this value slows down with increasing densification. As in the case of the one-by-one micrometer bed, it is expected that the simulation results will reach the bulk resistivity once there is only a single particle left in the bed.

3.2 Experiments

3.2.1 Furnace. The experiments were performed on the sintered pellets as described in the Methodology section, and the findings of the furnace experiments were previously presented in Ref. [22]. For each of the pellets, a range of currents applied to the circuit and the potential difference at each current measurement was observed. The resistance for the measurement was then taken as the slope of the current-voltage curve. The results of the experimental runs are collated in the plot in Fig. 8, which shows the corrected resistivity. Four-point probe geometric corrections were applied to the raw data to account for the thickness of the sample being much smaller than the spacing between the probe locations. These

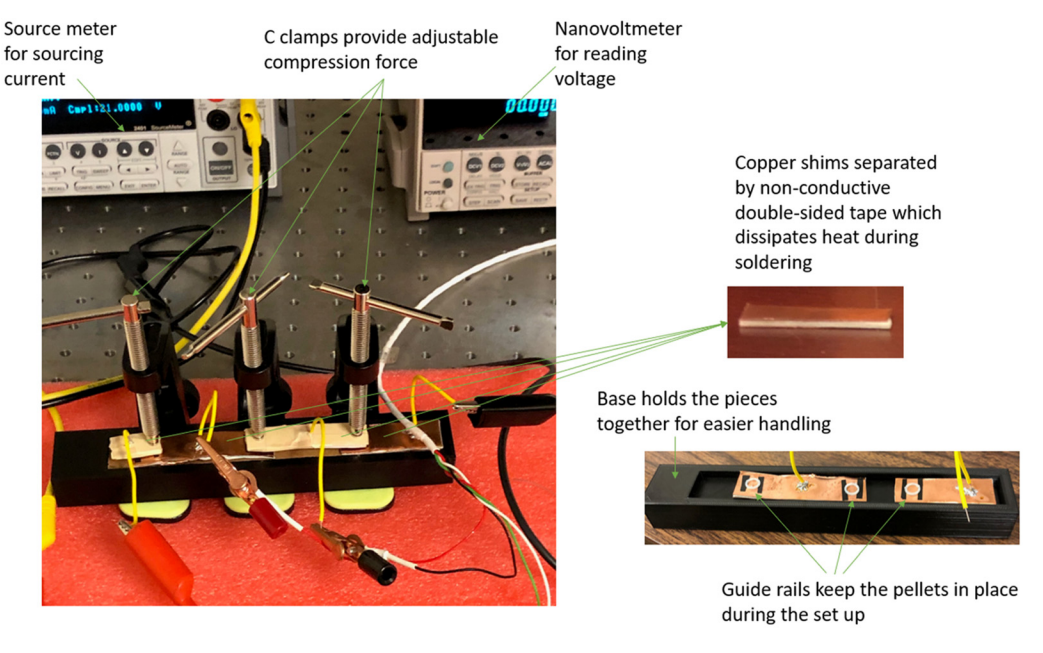


Fig. 5 Apparatus used for measuring the resistance of the sintered copper pellets [22]

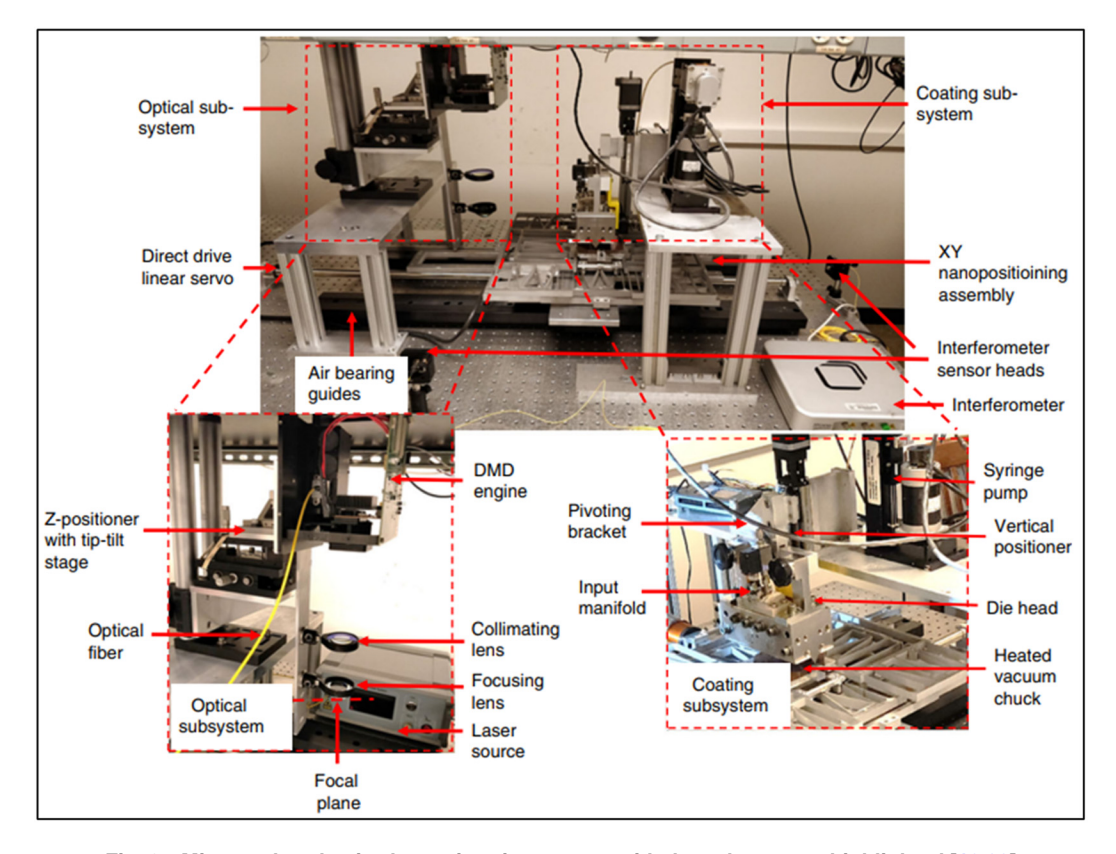


Fig. 6 Microscale selective laser sintering system with the subsystems highlighted [10,22]

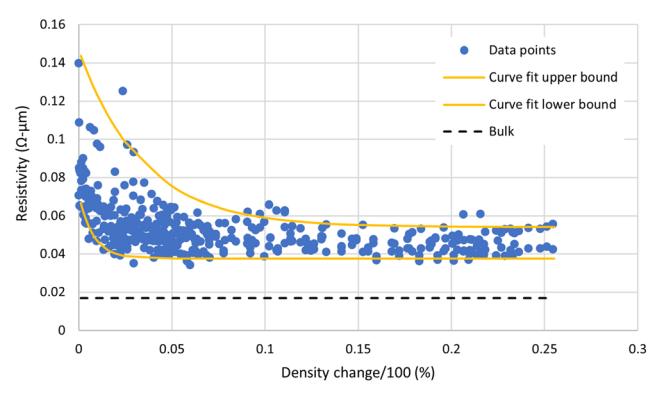


Fig. 7 Collated electrical resistivity curves for *x* and *y* current flow in multiple two-by-two micrometer beds

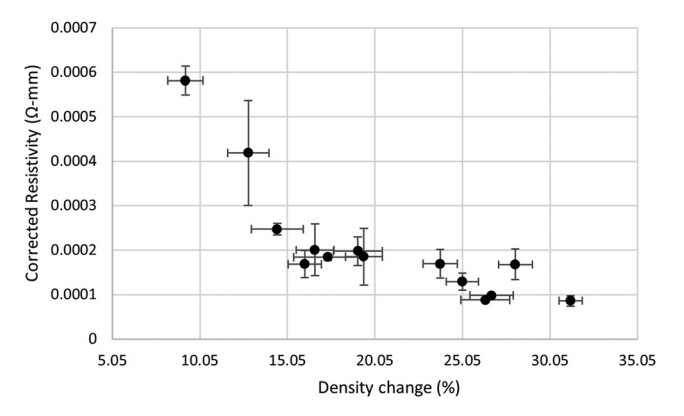


Fig. 8 Corrected resistivity as a function of densification [22]

corrections are a result of the boundaries in the relatively thin pellets which limit the possible current pathways [24,25].

For each densification point, three measurements are taken, and the value reported in the curve in Fig. 8 is the average of these three resistivity values and the error bars are the standard deviation of these measurements. The error bars in the densification change are found from propagating the error of each measurement taken to calculate the change in density. In general, the curve in Fig. 8 shows the expected trend of decreasing resistance with increasing degrees of densification of the pellet. The rate of decrease is steeper at lower rates of densification and becomes less steep as the degree of densification increases.

The resistivity in Fig. 8 asymptotes toward $8.58 \times 10^{-5}~\Omega$ -mm. The resistivity of bulk copper is $1.72 \times 10^{-5}~\Omega$ -mm, which means the steady-state resistivity recorded from the sintered pellets is roughly five times the value of bulk copper. A sintered ink resistivity of $9 \times 10^{-5}~\Omega$ -mm was quoted from the ink manufacturer; however, this value is dependent on the fabrication process. To determine how

close to fully sintered the pellets are, it is important to know what the final resistivity of the copper ink is for the furnace sintering fabrication process used for making these copper pellets. The minimum resistivity achievable with the ink was determined by spin coating a really thin layer of the copper nanoparticle ink onto a glass substrate and then heating the substrate with the ink up in the furnace for 5 h, flowing hydrogen and argon, as done with the pellets. After doing this, the resistance was measured. The resistivity measurements gave a minimum resistivity of $6.81 \times 10^{-5} \,\Omega$ -mm, 3.96 times the resistivity of bulk copper, for the ink sintered using the furnace sintering fabrication process. This minimum resistivity value was thus used to calculate the ratio of resistivity to fully sintered resistivity for comparison with the simulations and this comparison is shown in Fig. 9.

The results in Fig. 9 show that after the density increases by 15%, the simulations and the experiments are in good agreement, with the results from the experiments falling within the bounds from simulations. Prior to this densification though, the results from the

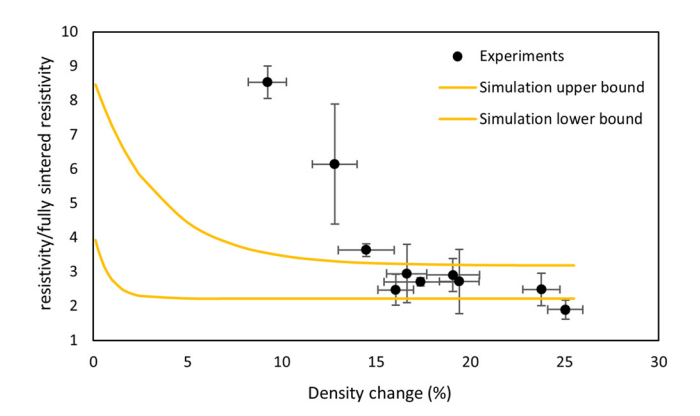


Fig. 9 Comparison of simulation and experiment electrical resistance results

experiments do not agree with the results from simulation. This is most likely a result of the polymer coatings, which encapsulate the copper nanoparticles. These coatings are present to prevent oxidation of the copper nanoparticles prior to sintering. The mass change plot in Fig. 10 shows that prior to achieving a 15% increase in density the mass changes by about 10% after sintering in the furnace. After a densification increase of 15% has been achieved though, the mass changes by a constant value of about 18%. The mass change values asymptote at 18%, with no higher mass change being seen with increasing changes in densification. The change in mass is calculated using the following equation:

$$mass change = \frac{mass before sintering - mass after sintering}{mass after sintering}$$
 (4)

The presence of the nanoparticle ink solvent and the coating around the nanoparticles used for the experiments leads to a higher mass than the mass of just the copper nanoparticles, so the true mass of the copper nanoparticles is the mass after sintering, once the solvent and coatings have decomposed. The lower change in mass in the lower densification regions in Figure 10 show that there are still some polymer coatings present in the pellets, which is why the electrical resistance values at this point are much higher. When the coating is completely gone, and the mass settles to the mass of just the copper nanoparticle pellets, seen in the results with higher densification, then the electrical resistance measured is not affected by the presence of the coatings and matches the results predicted by the simulations

As the goal of the simulation is to be able to predict the sintering of nanoparticles in the μ -SLS system, experiments were performed on

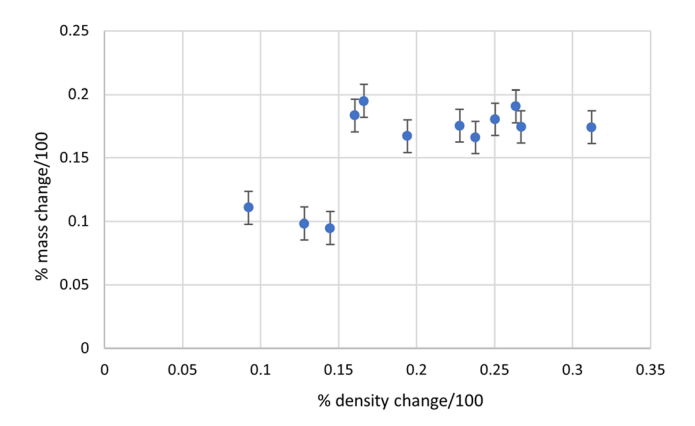


Fig. 10 Plot of the mass change of the sintered copper pellets before and after sintering in the furnace showing a step change in the mass at $\sim\!\!15\%$ densification indicating that this is the point where the surfactant coating is completely removed from the nanoparticles

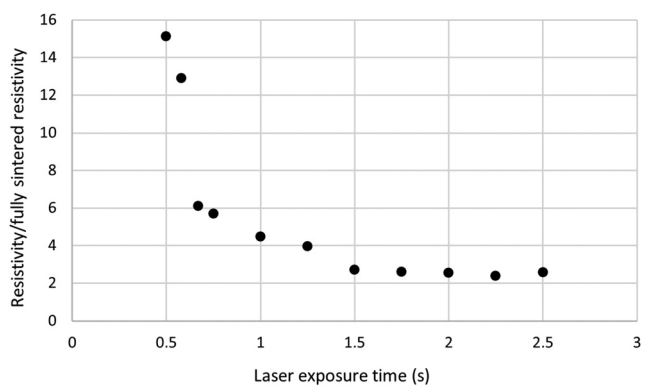


Fig. 11 Resistivity as a function of laser exposure time [22]

the μ -SLS system to determine how sintering time in the μ -SLS system scales to sintering time in the simulations in order to be able to accurately make predictions on the μ -SLS system using the simulations. Additionally, calibration was done between temperature and the laser sintering parameters to determine how the laser power maps to the temperature that the nanoparticles are being sintered at.

3.2.2 μ -SLS System. Once the relationship between the density and electrical resistance was measured from the furnace, the experiments were performed on the μ -SLS system and the resistivity ratio as a function of the laser exposure time was found. For these experiments, the laser was set at 55 A current and 20 V and the results are shown in Fig. 11.

To map these values back to the densification associated with each laser exposure time, the experimental data in Fig. 9 were fit to the exponential curve in Eq. (5), giving density change as a function of the resistivity. Once this relationship was found, the resistivity values from the μ -SLS system were mapped back to rates of densification [22]

density change
$$(\%) = 0.35e^{-0.43r} + 0.09$$
 (5)

where r in the equation is the ratio of resistivity against the fully sintered resistivity.

Additionally, to determine what temperature the laser sintering current of 55 A corresponds to, a calibration procedure was performed on the laser sintering results. This calibration outlined in Ref. [19] is done by minimizing the error between the furnace density versus time curves in [13] and the 55 A μ -SLS density versus time curve to determine which temperature gives the best fit (lowest error) to the μ -SLS results. This process showed that the 55 A laser sintering best fit furnace sintering at 550 °C with an average error of 0.7% and a calibration of 2.2 s of laser sintering time to 1 min of furnace sintering time. The results of this calibration are shown in Fig. 12.

With the map between temperature and laser power achieved, it is then possible to determine how the laser sintering time corresponds to the sintering simulation time. The process of calibrating simulation data curves to data curves from experiments has been previously outlined in [19]. Following this procedure for the results found in Fig. 12 gave a time calibration of 1,471,784 \pm 422,482 simulation timesteps per second of laser sintering time, which means that a single time-step in the simulation maps to about 0.68 \pm 0.19 microseconds of laser sintering time on the actual μ -SLS system.

When the furnace sintering density curve of the same temperature $550\,^{\circ}$ C is calibrated to the simulation results, the calibration value is $2,284,847\pm505,948$ simulation timesteps per minute of furnace sintering time [19]. If the calibration of $2.2\,\mu$ -SLS seconds to one furnace minute is applied to the simulation calibration of 2,284,847 simulation timesteps/minutes, this would give a calibration of 1,038,566 simulation timesteps per second of laser sintering time

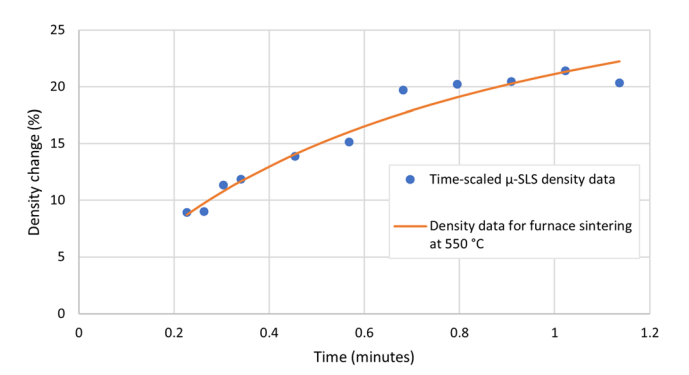


Fig. 12 Plot of time scaled μ -SLS results against furnace sintering results [22]

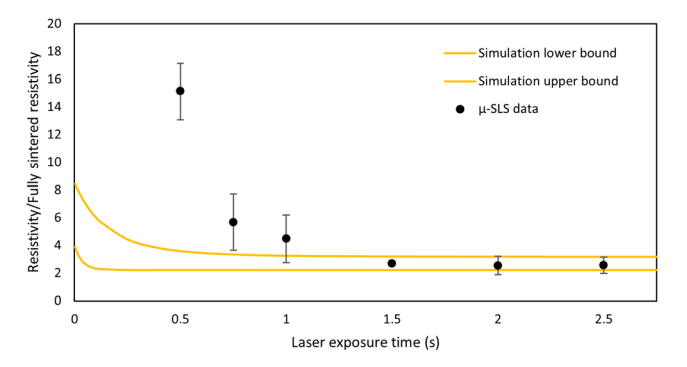


Fig. 13 Comparing electrical resistivity of the simulations with those from sintering with the μ -SLS system

which falls within 1.03 sigma of the mean in the actual time calibration distribution of $1,471,784\pm422,482$ simulation timesteps per second of laser sintering time derived from the results found in Fig. 12 above. The value falling within 1.03 sigma of the actual distribution provides additional validation for the calibration results as it shows that the calibration of simulation timesteps to laser sintering time, when derived through two different methods yield time calibration values belonging to the same distribution.

Using the calibration value for the μ -SLS system time, it is then possible to derive the relationship between the electrical resistance derived from simulations with that from the μ -SLS system. As the previous calibrations showed that sintering with the simulation at 550 °C corresponds to sintering with the laser sintering parameters of 55 A and 20 V, the electrical resistivity results from the simulation running with the input bed temperature set at 550 °C was used to predict the electrical resistivity curve for sintering with the μ -SLS system at 1100 W, by taking the plot of electrical resistivity against time from the simulations and applying the mean calibration of 1,471,784 simulation timesteps/seconds to the simulation time to yield a curve in the time domain of the μ -SLS sintering experiments. The actual resistivity curve from sintering with the μ -SLS system with these laser parameters are shown in Fig. 13 alongside the predictions from the simulation.

These results show a good match between the simulation and the experiments at the later stages of sintering, but there is a deviation between the measurements at the earlier sintering stages. As explained previously with the comparisons to furnace sintered measurements, this difference between the simulation and experimental measurements is a result of the presence of the solvent and coatings present in the nanoparticle ink. Once these have evaporated off, the results from the simulations have a closer match with those from the experiments with the μ -SLS system.

4 Conclusions and Future Work

In this paper, a tool for measuring the electrical resistance of a simulation bed has been presented. This tool takes in a simulation

bed under different stages of sintering and determines the electrical resistance of the bed using the resistance in the neck between particles as well as the bulk of the particles. Using this tool, a curve was found for the electrical resistance in 2 by 2 micrometer bed as a function of the density in the bed. This showed that the electrical resistance followed the expected trend of decreasing resistance with increasing densification. To show the validity of the simulation, experiments were performed on the same properties and then the results from the simulation were compared to those from the experiments.

To do this, the electrical resistance as a function of density from nanoparticles sintered in a furnace was determined experimentally. These measurements were performed using a four-point probe setup where current flows through two outer probes and the voltage drop across the inner probes is measured in order to cancel out the contact resistance associated with the samples being measured. Comparing the electrical resistance curves from experiments to that from simulations showed that in the valid range of the experiments, where there were no more coatings were present around the nanoparticles, the simulations matched the results from the experiments.

Finally, experiments were carried out to measure the electrical resistance of parts printed from the μ -SLS system. This was done to determine the connection between the laser sintering time and the sintering time in the simulations. In order for the simulations to be used to predict results on the actual μ -SLS system this calibration value had to be determined and it was shown that the calibration factor derived from this process matched the calibration factor derived from calibrating the furnace sintering time to laser sintering time, providing further validation for the simulations.

The results presented in this paper provide the building block of simulating nanoparticle sintering, allowing for the completion of the much larger goal of simulating the μ -SLS sintering process. The results presented in this paper as well as concurrently created nanoparticle thermal simulations [26,27] will be used to inform a much larger bed scale model. The bed scale model will be created using a finite element method (FEM) simulation where each element in the domain is akin to one of the microscale beds simulated with the nanoparticle sintering simulation which predict sintering as a function of temperature and time. Further work will be done to expand on the resistance experiments performed here for more laser powers, so that a full map can be derived between μ -SLS laser sintering parameters and furnace sintering temperature which will then be used as an input to the bed scale FEM simulation. Using this FEM simulation, it will be possible to model much larger size beds, with less computational expense, and derive the part properties which will help optimize the μ -SLS sintering process as well as reduce the formation of HAZ, which make it difficult to achieve near-net shaped parts.

Acknowledgment

This study was made possible through the Supercomputing resources of the Texas Advanced Computing Center. The authors would also like to thank NXP Semiconductors for the financial support provided.

Funding Data

 National Science Foundation (Grant No. 1728313; Funder ID: 10.13039/100000001).

Data Availability Statement

The datasets generated and supporting the findings of this article are obtainable from the corresponding author upon reasonable request.

References

 Moore, G. E., 2006, "Cramming More Components Onto Integrated Circuits, Reprinted From Electronics, Volume 38, Number 8, April 19, 1965, pp.114 ff.," IEEE Solid-State Circuits Society Newsletter, 11(3), pp. 33–35.

- [2] Allan, A., Edenfeld, D., Joyner, W. H., Kahng, A. B., Rodgers, M., and Zorian, Y., 2002, "2001 Technology Roadmap for Semiconductors," Computer, 35(1), pp. 42–53.
- [3] Koester, S. J., Young, A. M., Yu, R. R., Purushothaman, S., Chen, K.-N., La Tulipe, D. C., Rana, N., Shi, L., Wordeman, M. R., and Sprogis, E. J., 2008, "Wafer-Level 3D Integration Technology," IBM J. Res. Develop., 52(6), pp. 583–597.
- [4] Knickerbocker, J. U., Andry, P. S., Dang, B., Horton, R. R., Patel, C. S., Polastre, R. J., Sakuma, K., et al., 2008, "3D Silicon Integration," 58th Electronic Components and Technology Conference, Lake Buena Vista, FL, May 27–30, pp. 538–543
- [5] Vaezi, M., Seitz, H., and Yang, S., 2013, "A Review on 3D Micro-Additive Manufacturing Technologies," Int. J. Adv. Manuf. Technol., 67(5–8), pp. 1721–1754.
- [6] Vyatskikh, A., Delalande, S., Kudo, A., Zhang, X., Portela, C. M., and Greer, J. R., 2018, "Additive Manufacturing of 3D Nano-Architected Metals," Nat. Commun., 9(1), p. 593.
- [7] Hirt, L., Reiser, A., Spolenak, R., and Zambelli, T., 2017, "Additive Manufacturing of Metal Structures at the Micrometer Scale," Adv. Mater., 29 (17), p. 1604211.
- [8] Nelson, C., McAlea, K., and Gray, D., 1995, "Improvements in SLS Part Accuracy," Annual International Solid Freeform Fabrication Symposium, The University of Texas in Austin, Aug. 7–9, pp. 159–169.
- [9] Roy, N. K., Foong, C. S., and Cullinan, M. A., 2018, "Effect of Size, Morphology, and Synthesis Method on the Thermal and Sintering Properties of Copper Nanoparticles for Use in Microscale Additive Manufacturing Processes," Addit. Manuf., 21, pp. 17–29.
- [10] Roy, N. K., Behera, D., Dibua, O. G., Foong, C. S., and Cullinan, M. A., 2019, "A Novel Microscale Selective Laser Sintering (µ-SLS) Process for the Fabrication of Microelectronic Parts," Microsyst. Nanoeng., 5(1), p. 64.
- [11] Roy, N. K., Dibua, O. G., Jou, W., He, F., Jeong, J., Wang, Y., and Cullinan, M. A., 2018, "A Comprehensive Study of the Sintering of Copper Nanoparticles Using Femtosecond, Nanosecond, and Continuous Wave Lasers," ASME J. Micro Nano-Manuf., 6(1), p. 010903.
- [12] Roy, N. K., Foong, C. S., and Cullinan, M. A., 2016, "Design of a Micro-Scale Selective Laser Sintering System," Annual International Solid Freeform Fabrication Symposium, The University of Texas in Austin, Aug. 8–10, pp. 1495–1508.
- [13] Dibua, O. G., Yuksel, A., Roy, N. K., Foong, C. S., and Cullinan, M., 2018, "Nanoparticle Sintering Model: Simulation and Calibration Against Experimental Data," ASME J. Micro Nano-Manuf., 6(4), p. 041004.

- [14] Garg, R., Galvin, J., Li, T., and Pannala, S., 2012, "Documentation of Open-Source MFIX-DEM Software for Gas-Solids Flows," accessed Jan. 5, 2024, https://mfix.netl.doe.gov/doc/mfix-archive/mfix_current_documentation/dem_doc_2012-1.pdf
- [15] Dibua, O., Foong, C. S., and Cullinan, M., 2021, "Advances in Nanoparticle Sintering Simulation: Multiple Layer Sintering and Sintering Subject to a Heat Gradient," ASME Paper No. MSEC2021-63985.
- [16] Cahn, J. W., and Hilliard, J. E., 1958, "Free Energy of a Nonuniform System. I. Interfacial Free Energy," J. Chem. Phys., 28(2), pp. 258–267.
- [17] Cahn, J. W., 1961, "On Spinodal Decomposition," Acta Metall., 9(9), pp. 795–801.
- [18] Ginzburgh, V. L., and Landau, L. D., 1950, "On the Theory of Superconductivity," Zh. Eksp. Teor. Fiz., 20, pp. 1064–1082.
- [19] Dibua, O. G., Foong, C. S., and Cullinan, M., 2022, "Calibration Uncertainty in Nanoparticle Sintering Simulations," Manuf. Lett., 31, pp. 69–73.
- [20] Dibua, O., Foong, C. S., and Cullinan, M., 2022, "Electrical Resistance Metrology in Nanoparticle Sintering Simulations," ASME Paper No. MSEC2022-85997.
- [21] Zhang, Y., Wu, L., Guo, X., Jung, Y.-G., and Zhang, J., 2016, "Molecular Dynamics Simulation of Electrical Resistivity in Sintering Process of Nanoparticle Silver Inks," Comput. Mater. Sci., 125, pp. 105–109.
- [22] Dibua, O., Liao, A., Tasnim, F., Grose, J., Behera, D., Foong, C. S., and Cullinan, M., 2022, "A Study of the Electrical Resistivity of Sintered Copper Nano-particles," Proceedings of the 33rd Annual International Solid Freeform Eabrication Symposium, Hilton Austin Hotel in Austin, July 25–27, pp. 383–396.
- Fabrication Symposium, Hilton Austin Hotel in Austin, July 25–27, pp. 383–396.

 [23] Miccoli, I., Edler, F., Pfnür, H., and Tegenkamp, C., 2015, "The 100th Anniversary of the Four-Point Probe Technique: The Role of Probe Geometries in Isotropic and Anisotropic Systems," J. Phys.: Condens. Matter, 27(22), p. 223201.
- [24] Topsoe, H., 1968, "Geometric Factors in Four Point Resistivity Measurement," accessed Jan. 5, 2024, https://www.iiserkol.ac.in/~ph324/StudyMaterials/GeometricFactors4ProbeResistivity.PDF
- [25] Smits, F. M., 1958, "Measurement of Sheet Resistivities With the Four-Point Probe," Bell Syst. Tech. J., 37(3), pp. 711–718.
- [26] Grose, J., Dibua, O., Behera, D., Foong, C., and Cullinan, M., 2021, "Simulation and Characterization of Nanoparticle Thermal Conductivity for a Microscale Selective Laser Sintering System," ASME Paper No. MSEC2021-64048.
- [27] Grose, J., Dibua, O. G., Behera, D., Foong, C. S., and Cullinan, M., 2022, "Simulation and Property Characterization of Nanoparticle Thermal Conductivity for a Microscale Selective Laser Sintering System," ASME. J. Heat Mass Transfer-Trans. ASME, 145(5), p. 052501.